Structural-functional fingerprinting for abnormalities investigation in glioma patients

Maria Colpo[1,2], Erica Silvestri[2], Alessandro Salvalaggio[3], Diego Cecchin[1,4], Maurizio Corbetta[1,3], Alessandra Bertoldo*[1,2]

[1] Padova Neuroscience Center, University of Padova, Padova, Italy,
[2] Department of Information Engineering, University of Padova, Padova, Italy,
[3] Department of Neuroscience, University of Padova, Padova, Italy,
[4] Department of Medicine, Unit of Nuclear Medicine, University of Padova, Padova, Italy.

Corresponding author:
Alessandra Bertoldo: alessandra.bertoldo@unipd.it

Supplementary Information:

1. Supplementary Results

1.1 Participants

Patients were included in the study according to the following criteria: 1) first diagnosis of glioma (recurrences were excluded); 1) age 18 years old or older; 2) absence of other neurological or psychiatric disorders; 3) availability of standard magnetic resonance imaging (MRI) acquisitions, including pre-and post-contrast T1-weighted sequences, T2-weighted, fluid-attenuated inversion recovery, resting state-functional MRI (rs-fMRI) and diffusion MRI (dMRI); 4) absence of macroscopic metallic artifacts in MR images.

Supplementary Table S1. Single patient's demographic and clinical information. *From the left, for each patient, there are demographics information, lesion histology, lesion type classification (WHO 2016[1] classification), lesion hemisphere position, lesion lobe position, lesion volume and tumour volume. (Hemi=involved hemisphere, T+O volume=extent of the tumour + oedema segmentation, T volume=extent of the tumour segmentation, CC= corpus callosum, F=frontal lobe, L=left, N.A.= not available, O=occipital lobe, P=parietal lobe, R=right, T=temporal lobe, WT=wild type, \=not measured).*

Patient ID	Age	Gender	Histology	Classification	IDH1	Hemi	Lobe	T+O volume [cm^3]	T volume [cm^3]
1	74	M	Diffuse glioneuronal tumour	High grade	\	L	T	30	5
2	25	F	Oligodendroglioma	Low grade	mutant	L	F	53,5	39,4
3	43	M	Glioblastoma	High grade	WT	L	F	81,1	0,4
4	56	F	Intracranial mesenchymal	Low grade	\	L	F	6,8	6,8
5	69	M	Glioblastoma	High grade	WT	L	T	70,1	66,2
6	83	M	N.A.	N.A.	N.A.	L	P-T	11,7	10
7	67	F	Glioblastoma	High grade	WT	L	P	19,4	6,7
8	83	F	Glioblastoma epithelioid	High grade	WT	L	F-P	60,8	36,6
9	37	F	Astrocytoma	Low grade	mutant	L	F	11	11
10	56	M	Glioblastoma	High grade	mutant	L	F	127	88,8
11	75	F	Glioblastoma	High grade	WT	L	T	80,4	8,1
12	46	F	Glioneuronal neoplasm	High grade	mutant	L	F-insular	83,1	83,1

13	77	M	Glioblastoma	High grade	WT	L	T	103	85,4
14	57	M	Glioblastoma	High grade	WT	L	O-T	50,9	43,1
15	49	F	Glioblastoma	High grade	WT	L	T	36,8	34,5
16	74	F	Glioblastoma	High grade	WT	L	F	16,4	3,4
17	56	F	Glioblastoma	High grade	WT	L	T	6,1	6,1
18	49	M	Glioblastoma	High grade	WT	L	T	13,1	7,8
19	54	F	Glioblastoma	High grade	WT	L	T	25,7	24,3
20	67	M	Glioblastoma	High grade	WT	L	F	49,3	48,1
21	50	M	Glioblastoma	High grade	N.A.	L	F	95,1	83,3
22	70	M	Glioblastoma	High grade	WT	L	T	18,9	16,3
23	58	F	Glioblastoma	High grade	WT	R	F-insular + splenium	76	73,9
24	42	M	Glioblastoma	High grade	mutant	R	F	139,2	123
25	32	F	Glioblastoma	High grade	WT	R	Thalamus	78,3	53,3
26	48	F	Glioblastoma	High grade	WT	R	T + optic tract	56,4	53,4
27	61	M	Diffuse astrocytoma	Low grade	mutant	R	T	12,4	7,4
28	57	M	Glioblastoma	High grade	WT	R	F	191,6	108,3
29	80	M	Glioblastoma	High grade	WT	R	O-T	17,7	17,3
30	36	F	Not Otherwise Specified	Low grade	\	R	T	5,7	5,7
31	83	M	N.A.	N.A.	N.A.	R	P-T-O	65,3	19
32	51	M	Multinodular and vacuolating	Low grade	\	R	P	14,9	14,9
33	64	F	Glioblastoma	High grade	WT	R	T-P	155,9	155,9
34	73	M	Glioblastoma	High grade	WT	R	F	122,3	44,7
35	57	F	Glioblastoma	High grade	WT	R	F	112,4	99,5
36	64	F	Glioblastoma	High grade	WT	R	F	125,1	62,6
37	36	M	Glioblastoma	High grade	WT	B	F, CC	128,9	51,4
38	74	M	Diffuse large B-cell lymphoma	High grade	\	B	F-P + splenium	27,3	8,2
39	64	M	Glioblastoma	High grade	WT	B	F-insular R + CC L	67,9	54
40	68	M	Glioblastoma	High grade	WT	B	F-T-insular + cingulate	134,2	127,5

41	73	M	N.A.	N.A.	N.A.	B	splenium CC	37,3	36,9

1.2 Examining the relationship between gliomas and integrated and individual connectivity modalities

In Supplementary Figure S1, patients with a left lesion exhibit a higher impact on left hemisphere areas for networks in overlap with the lesion (overlay with tumour (T) in Panel A, overlay with oedema (O) in Panel B). It is worth noting that FC, SNFmicro and SCnos contributed less, in order, to the IC. Panel C, representing only altered networks overlapping with healthy tissues, provides an overview of higher alterations in the contralateral hemisphere. Likewise, SCnos presented a null contribution to the IC. Conversely, in Supplementary Figure S2, patients with a right lesion show a higher impact on right hemisphere areas for networks in overlap with the lesion (overlay with tumour (T) in Panel A, overlay with oedema (O) in Panel B). Of note is the reduced ordered contribution of FC, SNFmicro, and SCnos to the IC. Panel C, which exclusively displays altered networks overlapping with healthy tissues, offers a summary of increased alterations in the contralateral hemisphere. In the same way in Supplementary Figure S1 and Supplementary Figure S2, SCnos presents a negligible contribution to the IC.

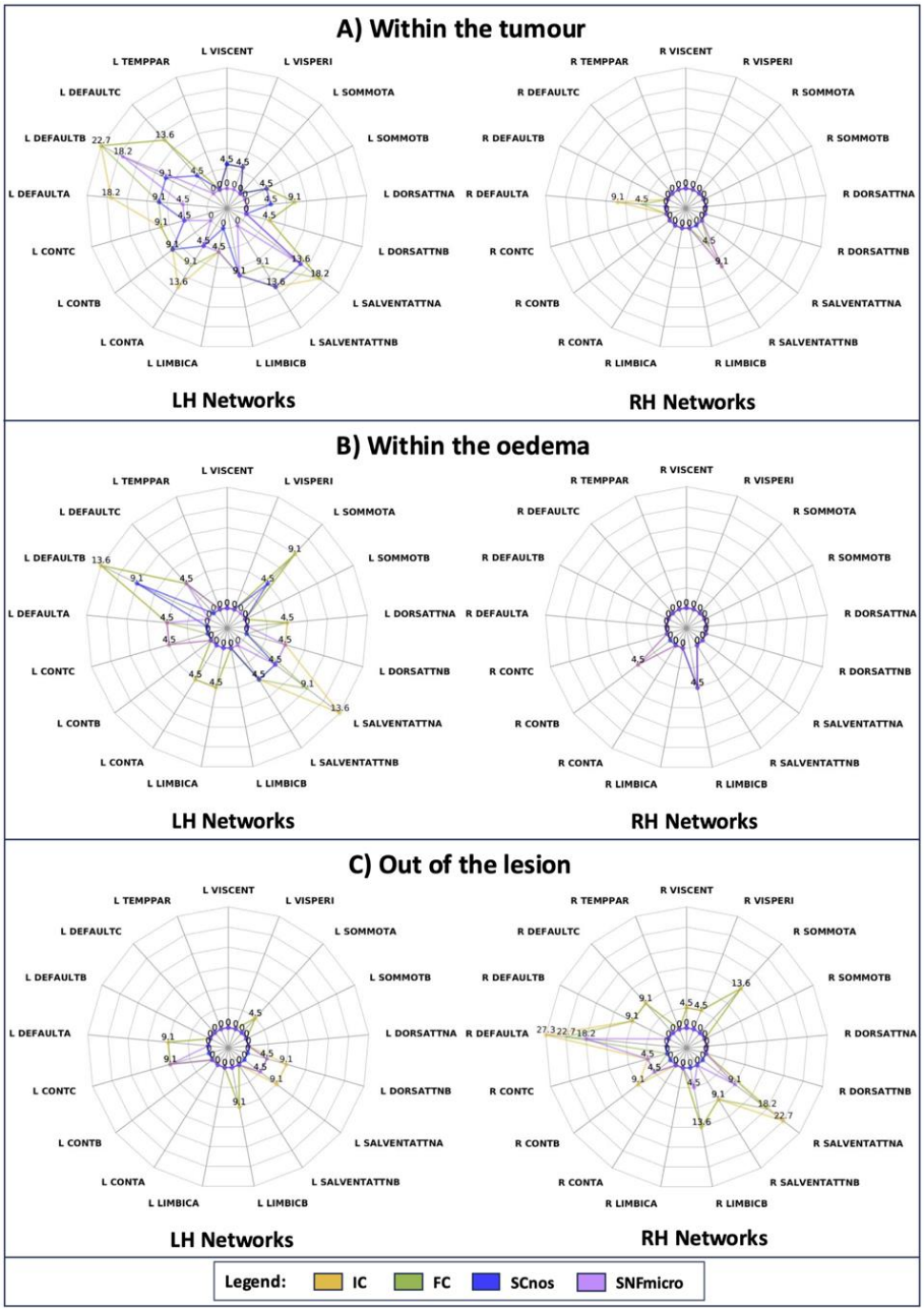

Supplementary Figure S1. Overall percentage of patients with left hemisphere lesion with IC, FC, SCnos and SNFmicro altered networks. *In general, the spider plot represents the percentage of patients, with a lesion on the left hemisphere, with altered connectivity associated to each Yeo Network. Networks are grouped according to left and right hemisphere (left and right side of the image). For each pair of spider plots displayed in the same row, values range is the same. As illustrated in the legend, IC mode in yellow, FC mode in green, SCnos mode in blue, SNFmicro mode in purple. In A), the percentage of patients with altered network overlapping with the tumour (T) is depicted. In B), the percentage of patients with altered network in overlap with the oedema (O) is displayed. In C), the percentage of patients with altered network out of the lesion is showed. VisCent = Visual Central network; VisPeri = Visual Peripheral network; SomMotA = Somatomotor-A network; SomMotB = Somatomotor-B network; DorsAttnA = Dorsal Attention-A network; DorsAttnB = Dorsal Attention-B network; SalVentAttnA = Salience/Ventral Attention-A network; SalVentAttB = Salience/Ventral Attention-B network; LimbicB = Limbic-B network; LimbicA = Limbic-A network; ControlA = Control-A network; ControlB = Control-B network; ControlC = Control-C network; DefaultA = Default-A network; DefaultB = Default-B network; DefaultC = Default-C network; TempPar = Temporal Parietal network.*

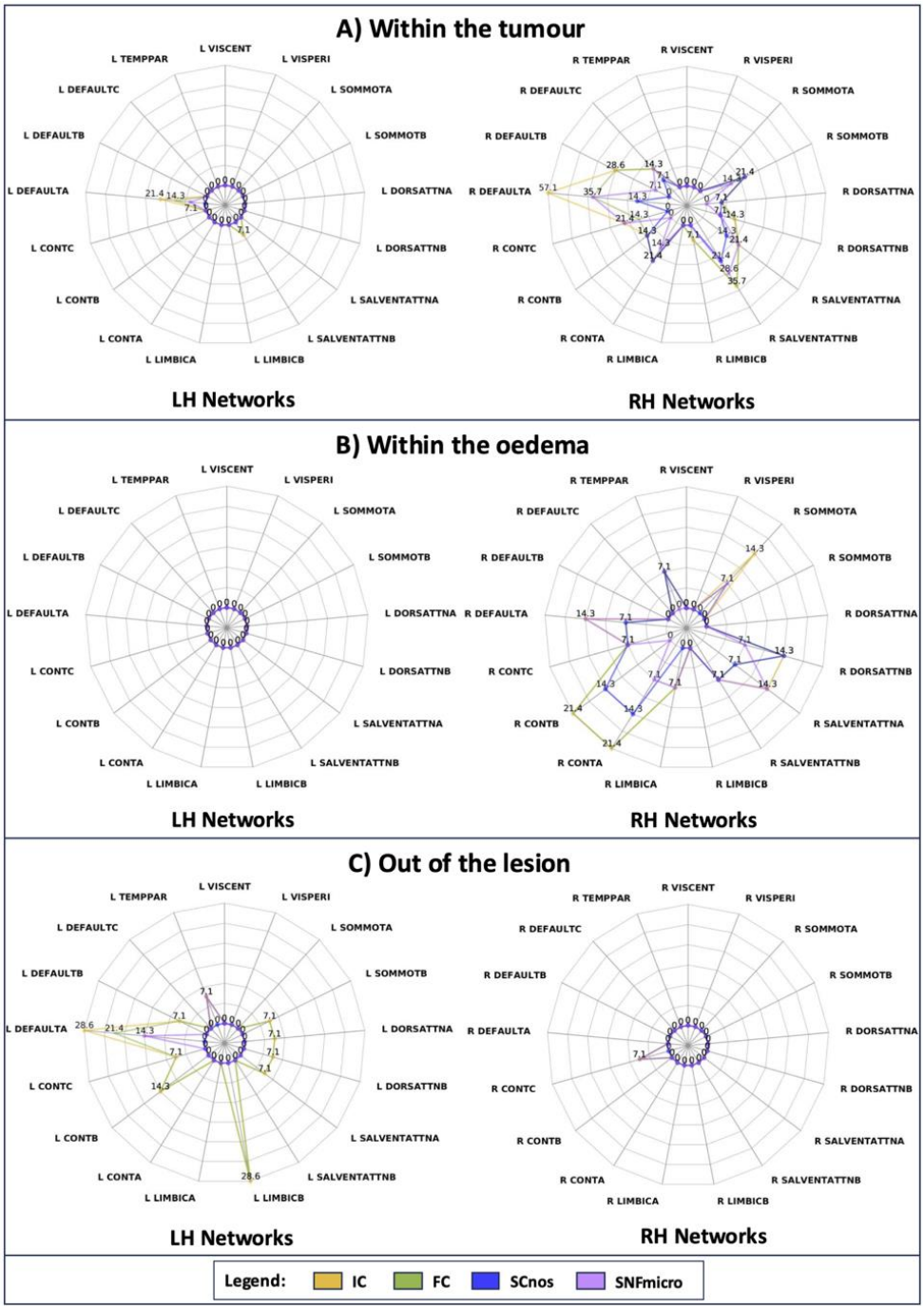

Supplementary Figure S2. Overall percentage of patients with right hemisphere lesion with IC, FC, SCnos and SNFmicro altered networks. *In general, the spider plot represents the percentage of patients, with a lesion on the right hemisphere, with altered connectivity associated to each Yeo Network. Networks are grouped according to left and right hemisphere (left and right side of the image). For each pair of spider plots displayed in the same row, values range is the same. As illustrated in the legend, IC mode in yellow, FC mode in green, SCnos mode in blue, SNFmicro mode in purple. In A), the percentage of patients with altered network overlapping with the tumour (T) is depicted. In B), the percentage of patients with altered network in overlap with the oedema (O) is displayed. In C), the percentage of patients with altered network out of the lesion is showed. VisCent = Visual Central network; VisPeri = Visual Peripheral network; SomMotA = Somatomotor-A network; SomMotB = Somatomotor-B network; DorsAttnA = Dorsal Attention-A network; DorsAttnB = Dorsal Attention-B network; SalVentAttnA = Salience/Ventral Attention-A network; SalVentAttB = Salience/Ventral Attention-B network; LimbicB = Limbic-B network; LimbicA = Limbic-A network; ControlA = Control-A network; ControlB = Control-B network; ControlC = Control-C network; DefaultA = Default-A network; DefaultB = Default-B network; DefaultC = Default-C network; TempPar = Temporal Parietal network.*

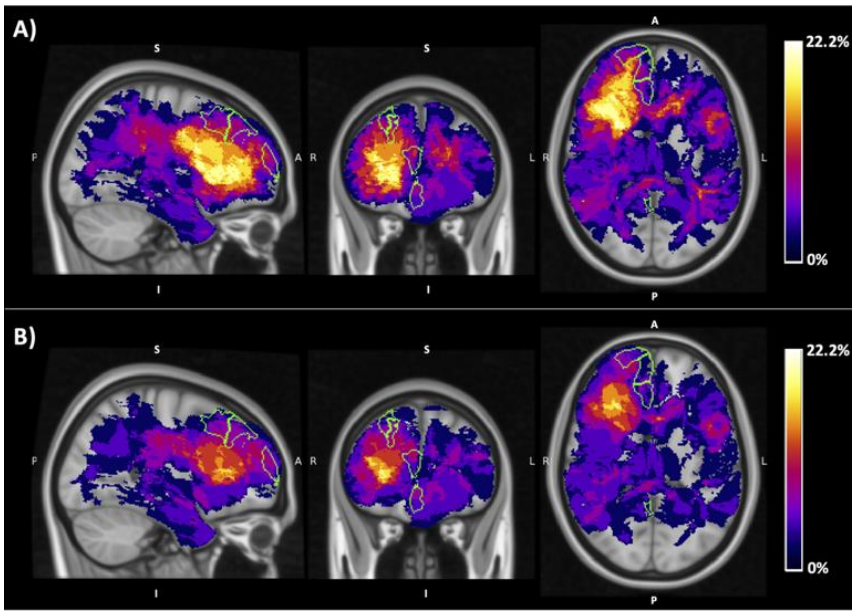

Supplementary Figure S3. Overlap between lesion frequency map and most frequently altered regions within the tumour. *Overlap between Right Default-A Network region and lesion(T+O)/tumour(T) frequency map (Panel A/B). Regions with the highest overlap in lesion(T+O)/tumour(T) occurrences are visualized in bright yellow. The Right Default-A Network is the region, overlapping with the tumour (T), most frequently altered among the patients. Regions of the Right Default-A Network are overlaid in bright green to visualize the overlap of patients' lesion(T+O)/tumour(T) distribution and network representation. Maps are superimposed to the MNI atlas (grey scale). Radiological convention.*

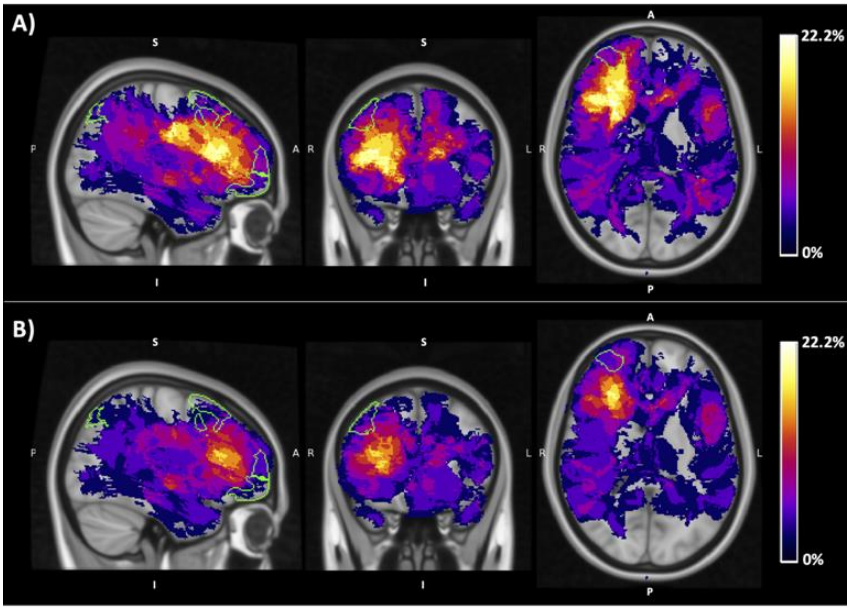

Supplementary Figure S4. Overlap between lesion frequency map and most frequently altered regions within the oedema. *Overlap between Right Control-B Network region and lesion(T+O)/tumour(T) frequency map (Panel A/B). Regions with the highest overlap in lesion(T+O)/tumour(T) occurrences are visualized in bright yellow. The Right Control-B Network is the region, overlapping with the oedema (O), most frequently altered among the patients. Regions of the Right Control-B Network are overlaid in bright green to visualize the overlap of patients' lesion(T+O)/tumour(T) distribution and network representation. Maps are superimposed to the MNI atlas (grey scale). Radiological convention.*

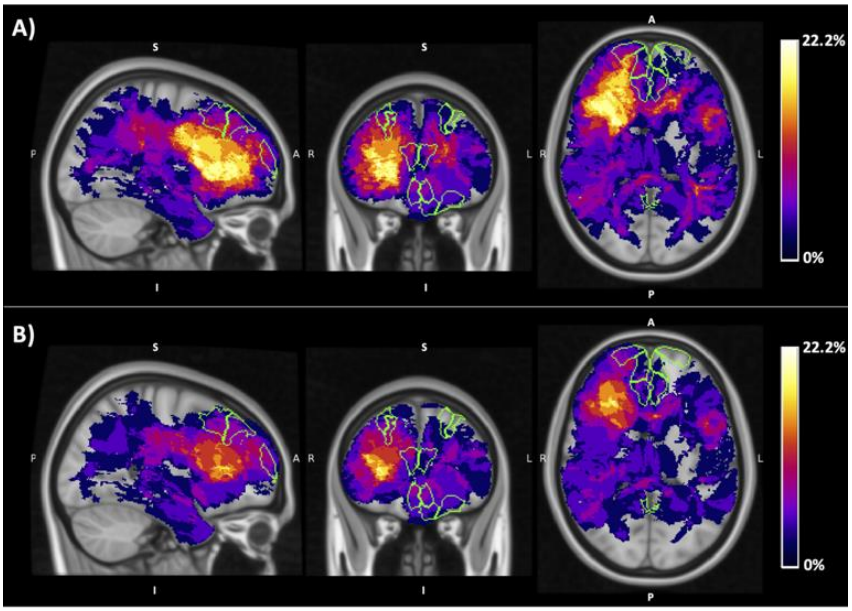

Supplementary Figure S5. Overlap between lesion frequency map and most frequently altered regions out of the lesion. *Overlap between Right Default-A, Left Default-A and Left Limbic-B Network regions and lesion(T+O)/tumour(T) frequency map (Panel A/B). Regions with the highest overlap in lesion(T+O)/tumour(T) occurrences are visualized in bright yellow. The Right Default-A, Left Default-A and Left Limbic-B Networks are the regions, without the lesion (T+O), most frequently altered among the patients. Regions of the Right Default-A, Left Default-A and Left Limbic-B Networks are overlaid in bright green to visualize the overlap of patients' lesion(T+O)/tumour(T) distribution and network representation. Maps are superimposed on the MNI atlas (greyscale). Radiological convention.*

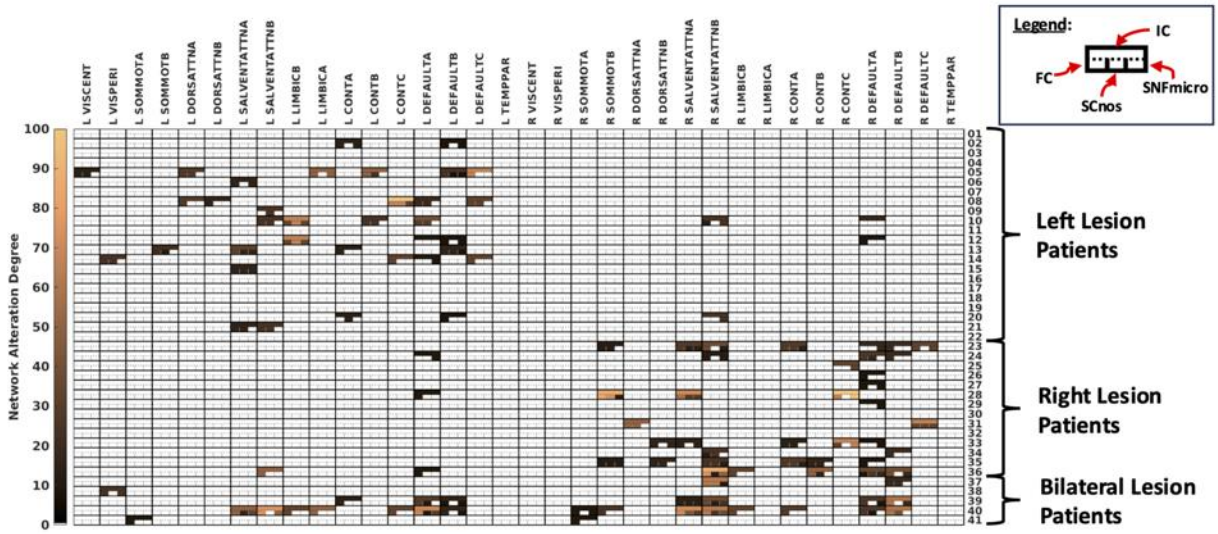

Supplementary Figure S6. Network Alteration Degree distribution of IC, FC, SCnos and SNFmicro within the tumour. *Network Alteration Degree derived from IC, FC, SCnos and SNFmicro, for networks overlapping with the tumour core (T). Values associated to different connectivity modality are displayed as illustrated in the legend. Patients are grouped according to lesion hemisphere position. From the top: left lesion patients, right lesion patients, bilateral lesion patients. Results are presented for a R^2 threshold equal to 0.25. VisCent = Visual Central network; VisPeri = Visual Peripheral network; SomMotA = Somatomotor-A network; SomMotB = Somatomotor-B network; DorsAttnA = Dorsal Attention-A network; DorsAttnB = Dorsal Attention-B network; SalVentAttnA = Salience/Ventral Attention-A network; SalVentAttB = Salience/Ventral Attention-B network; LimbicB = Limbic-B network; LimbicA = Limbic-A network; ControlA = Control-A network; ControlB = Control-B network; ControlC = Control-C network; DefaultA = Default-A network; DefaultB = Default-B network; DefaultC = Default-C network; TempPar = Temporal Parietal network.*

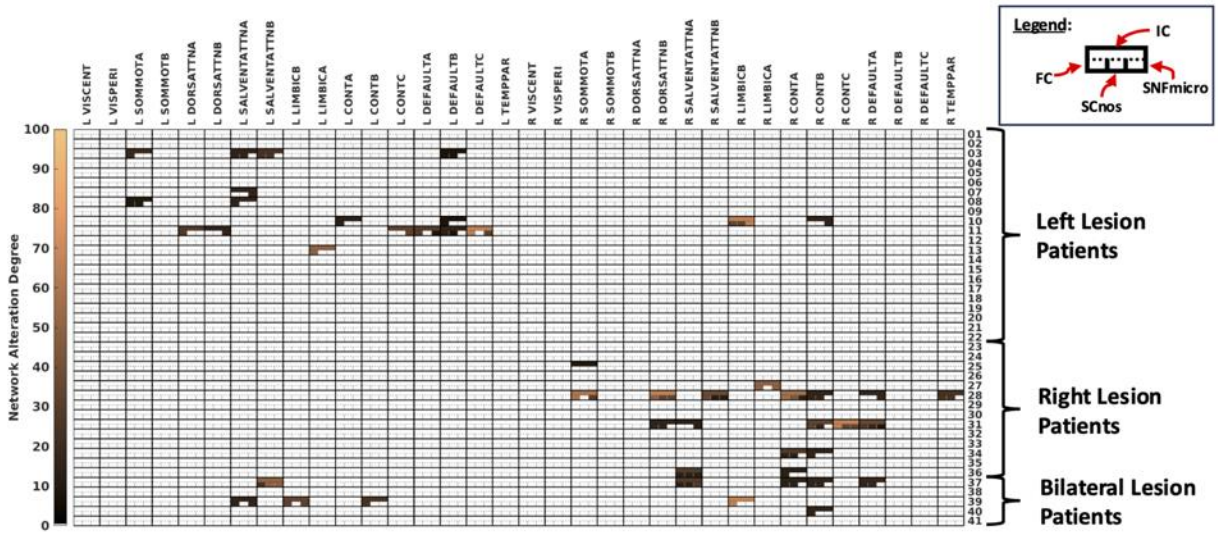

Supplementary Figure S7. Network Alteration Degree distribution of IC, FC, SCnos and SNFmicro within the oedema. *Network Alteration Degree derived from IC, FC, SCnos and SNFmicro, for networks overlapping with the oedema (O). Values associated to different connectivity modality are displayed as illustrated in the legend. From the top: left lesion patients, right lesion patients, bilateral lesion patients. Patients are grouped according to lesion hemisphere position. Results are presented for a R^2 threshold equal to 0.25. VisCent = Visual Central network; VisPeri = Visual Peripheral network; SomMotA = Somatomotor-A network; SomMotB = Somatomotor-B network; DorsAttnA = Dorsal Attention-A network; DorsAttnB = Dorsal Attention-B network; SalVentAttnA = Salience/Ventral Attention-A network; SalVentAttB = Salience/Ventral Attention-B network; LimbicB = Limbic-B network; LimbicA = Limbic-A network; ControlA = Control-A network; ControlB = Control-B network; ControlC = Control-C network; DefaultA = Default-A network; DefaultB = Default-B network; DefaultC = Default-C network; TempPar = Temporal Parietal network.*

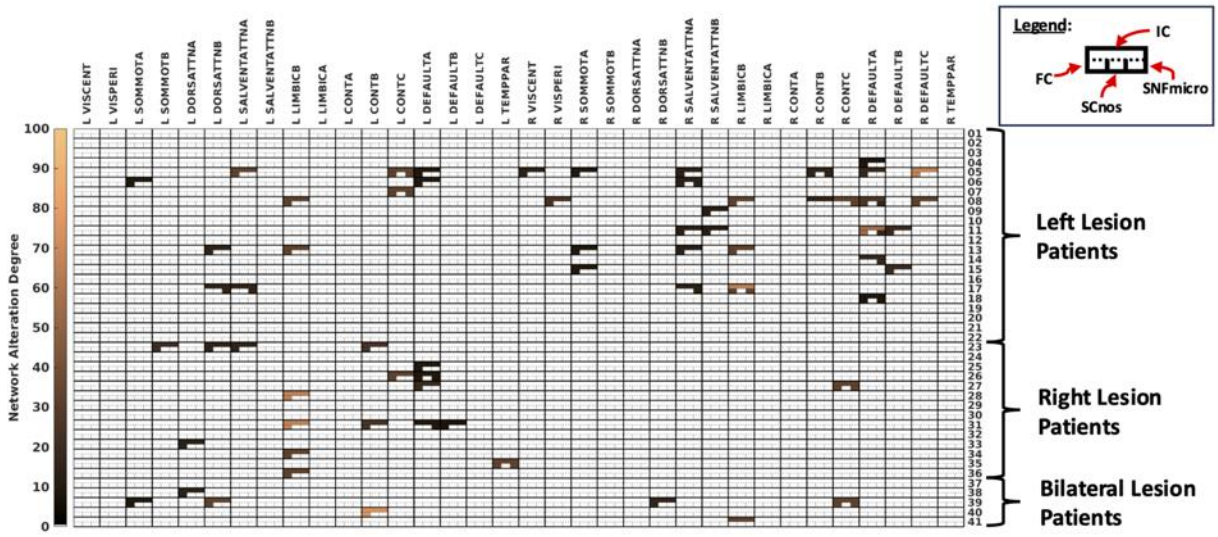

Supplementary Figure S8. Network Alteration Degree distribution of IC, FC, SCnos and SNFmicro out of the lesion. *Network Alteration Degree derived from IC, FC, SCnos and SNFmicro, for networks overlapping with healthy tissues. Values associated to different connectivity modality are displayed as illustrated in the legend. Patients are grouped according to lesion hemisphere position. From the top: left lesion patients, right lesion patients, bilateral lesion patients. Results are presented for a R^2 threshold equal to 0.25. VisCent = Visual Central network; VisPeri = Visual Peripheral network; SomMotA = Somatomotor-A network; SomMotB = Somatomotor-B network; DorsAttnA = Dorsal Attention-A network; DorsAttnB = Dorsal Attention-B network; SalVentAttnA = Salience/Ventral Attention-A network; SalVentAttB = Salience/Ventral Attention-B network; LimbicB = Limbic-B network; LimbicA = Limbic-A network; ControlA = Control-A network; ControlB = Control-B network; ControlC = Control-C*

network; DefaultA = Default-A network; DefaultB = Default-B network; DefaultC = Default-C network; TempPar = Temporal Parietal network.

2. Supplementary Methods

2.1 Data acquisition

The MRI protocol included a set of anatomical images, comprising of a 3D T2-weighted (T2w) FLAIR image (TR/TE 5000/395 ms; voxel size 1x1x1 mm^3; FOV 250x250 mm^2), two 3D T1-weighted (T1w) MPRAGE (TR/TE 2400/3.2 ms; voxel size 1x1x1 mm^3; FOV 256x256 mm^2; 160 slices) acquired both before and after contrast agent injection and a T2w image (TR/TE 3200/536 ms; voxel size 1x1x1 mm^3; FOV 256x256 mm^2; 160 slices). In addition, a multi-shell dMRI protocol featured 100 diffusion-weighted images (DWIs) (TR/TE 5355/104 ms; voxel size 2x2x2 mm^3; FOV 220x220 mm^2; 68 slices; multiband accelerator factor=2) divided in the following shells: 10 images at b=0 s/mm^2, 30 DWIs at b-value=710 s/mm^2 and 60 DWIs at b-value=2855 s/mm^2. The diffusion protocol in place was adapted from the work of Zhang and colleagues[7]. Each diffusion direction was acquired with two reversed phase encoding directions, i.e., anterior-posterior and posterior-anterior directions, to enable the distortion correction process described in the following section. In addition, functional imaging comprised rs-fMRI scans acquired with a T2*-weighted gradient-echo echo planar imaging (EPI) sequence (TR = 1260 ms, TE = 30 ms, Flip Angle = 68°, FOV = 204 × 204 mm2, voxel size = 3 × 3 × 3 mm3, iPAT = 0, multi-band acceleration factor (MBAccFactor) = 2, volumes = 750, TA = 16:03 min, phase encoding direction antero-posterior) and two spin echo-EPI acquisitions with reverse phase encoding (TR = 4200 ms, TE = 70 ms, Flip Angle = 90°, FOV = 204 × 204 mm2, voxel size = 3 × 3 × 3 mm3, TA = 8.4 s) for EPI distortion correction purposes.

2.2 Tumour segmentation and structural pre-processing

The T1w image of each patient underwent a structural preprocessing pipeline which consisted of the following steps: bias field correction (N4BiasFieldCorrection[8]), skull-stripping (Multi-Atlas Skull Stripping[9]) and tissue segmentation (into GM, WM and corticospinal fluid (CSF) with the unified segmentation tool[10] of the Statistical Parametric Mapping, SPM12 v. 7771). Following these steps, the T1w image was normalized to the symmetric MNI152 2009c atlas[11] with a diffeomorphic transformation computed in ANTs. In the computation of this normalization, we excluded the tumoral lesion mask from contributing to the registration cost function, as suggested by[12].

2.3 Functional imaging processing

The Functional pre-processing of rs-fMRI data included slice timing[13], readout distortion (FSL's TOPUP[14]) and motion (FSL's *mcflirt*[15]) correction, a non-linear mapping to the symmetric MNI152 2009c atlas[11] through the subject-specific T1w (via FSL's boundary-based registration[16]) and high pass filtering (cut-off frequency: 0.008 Hz). As a second step, the GIFT toolbox (http://trendscenter.org/software/gift/) was used to decompose the functional pre-processed images. Scanner artifacts' spurious variance was regressed out from the patients' pre-processed data using an independent component approach (ICA)[17]. Then, the independent components related to the sequence MB factor or broad head movement artifacts were manually identified and regressed out from the original pre-processed data[18,19]. Additional information regarding the selection process of independent components can be found in[20]. Moreover, 10 principal components related to CSF and WM signal (5 from WM, 5 from CSF) were regressed out from rs-fMRI time-series. This regression process also included the removal of the six standard head motion parameters[21]. The next step included a low pass filter (cut-off frequency: 0.11 Hz). Finally, to quantify the subject-specific head motion during the scan, frame-wise displacement was computed as defined in[22]. Eventually, subjects affected by high head motion (less than 400 volumes with mean FD<0.4 mm) were discarded.

2.4 Diffusion imaging processing, tractogram generation and microstructure estimation

dMRI images underwent manual quality control, to identify and remove diffusion volumes affected by interslice instabilities[23] (such as Venetian blinds artifacts[24]). The following steps of pre-processing were executed within the MRtrix3 software[25]. The pipeline sequence featured: 1) random-matrix based denoising via the *dwidenoise* command[26] and a B0-inhomogeneities joint correction, 2) subject motion and 3) eddy currents via *dwifslpreproc*[14,27]. Finally, T1w segmentation images (including GM, subcortical parcellation, lesion, and tumour masks) were aligned to the naïve mean B0 volume using ANTs[28]. This alignment was achieved by employing an affine transformation that had been previously calculated based on the patient's original T1-weighted image.

Individual brain tractogram was generated as follows. At first, multi-shell multi-tissue spherical deconvolution approach was performed to recover voxel-wise orientation distribution functions for each WM, GM and CSF voxel[29].

Neurite Orientation Dispersion and Density Imaging (NODDI) and Diffusion Kurtosis Imaging (DKI) models were fitted on the dataset applying off-the-shelf toolboxes publicly available (NODDI[30] and https://cai2r.net/resources/diffusion-kurtosis-imaging-matlab-toolbox/-DKI). Diffusion Tensor Imaging (DTI) models were fitted with *dtifit* command of FSL software[4]. All microstructure maps underwent outlier checking: if voxels' values were outside the respective established literature range, voxels' outlier values were substituted by new values, provided by the application of a spatial median filter on the respective microstructure map.

2.5 Structural and functional connectivity computation

The parcellation was brought into the individual B0 space with a single interpolation step that used a unique transform which comprised the registration from the MNI152 atlas to the individual T1w image, from this to the individual T2w image and finally a linear transform between the T2w and the B0 image. Yan cortical atlas was also directly co-registered to the symmetric MNI152 2009c atlas.

2.6 Validation of pseudo-healthy reference using an independent healthy dataset

The pseudo-healthy reference structure of SCnos has been compared to group SC patterns observed in healthy individuals. The independent healthy data collection was derived from the Human Connectome Project (HCP) in Aging (HCP-Aging)[2] project. HCP-A data acquisition and sharing have been approved by the HCP parent IRB. All HCP participants gave full written informed consent prior to the data collection, following Washington University–University of Minnesota (WU-Minn HCP) Consortium ethical guidelines.

200 subjects (59.29±14.28 years, 112/88 M/F) were selected from the HCP-Aging dataset, to match the oncological dataset sex and age range. Subjects included these images: clinical structural imaging (T1w and T2w) and dMRI. HCP-Aging project enrolled individuals in the age range [36-100] years, according to the second HCP release (Lifespan HCP 2.0 Data Release) instructions and collected healthy brains. To be part of the study, participants must not present the following criteria: diagnosis or treatment for major neuropsychiatric or neurological disorders, depression, cognitive impairments identification, learning disabilities, or severe medical conditions[2].

HCP protocol acquisition: The HCP-A imaging protocol was acquired with a standard Siemens 3T Prisma scanner with a 32-channel head coil. Structural T1-weighted and T2-weighted images were scanned with a multi-echo magnetization-prepared gradient-echo sequence. Bi-shell dMRI protocol featured four consecutive dMRI runs, sampled with 185 diffusion-weighting directions (92 DWIs at b-value=1500 s/mm^2 and 93 DWIs at b-value=3000 s/mm^2), each acquired twice with opposite phase encoding direction (AP and PA) to facilitate robust correction of distortions. 28 b-value=0 s/mm^2 volumes equally interspersed across the four runs (TR = 3230 ms; voxel size 1.5x1.5x1.5 mm3, MB = 4). Rs-fMRI images were collected using a 2D multiband gradient-recalled echo EPI sequence (TR = 800 ms; TE = 37 ms; flip angle = 52°; voxel size = 2.0 × 2.0 × 2.0 mm; volumes = 478; multiband factor = 8). Further details about the acquisition protocol and choices are reported in[2].

HCP diffusion pre-processing, tractogram generation and structural connectivity matrix generation: HCP-A subjects underwent a first dMRI processing following the minimal processing pipeline[3] specifically developed for HCP data collection. Tractogram generation followed the same procedures as outlined for the oncological dataset described in Supplementary Material 2.4, omitting the use of the lesion mask in the 5TT segmented tissue image due to the healthy brain condition. For HCP-Aging subjects, Yan parcellations were aligned to the individual T1w using FSL software[4], with transformations previously estimated by the HCP minimal processing pipeline[3]. Finally, as done for oncological patients, SC matrices based on *Number of Streamlines* (SCnos) were generated. The process involved superimposing the atlas-based parcellation on the individual whole-brain tractogram and assessing the NOS in the tractogram connecting each pair of parcels. The result was a 200x200 matrix. One-streamline connections were set to zero.

Graph measures derivation: The group-median SCnos HCP matrices were computed by calculating the median across the individual HCP SCnos matrices, with connections containing only one streamline removed according to the procedure described for oncological matrices. The SCnos pseudo-healthy and median HCP-SCnos matrices were then thresholded separately, retaining only connections associated with SCnos weights above the 80th percentile of the median SCnos weight distribution[5]. As highlighted in de Brito Robalo et al. [6], applying thresholding is expected to lead to more consistent network architectures by reducing false positives and improving precision in network analysis. Graph theory measures were applied to both the median HCP-SCnos and SCnos pseudo-healthy matrices after thresholding, yielding comparable results. Notably, global efficiency was identical for both matrices (G_onco = 0.59, G_HCP = 0.59), and modularity values were similar (M_onco = 0.35, M_HCP = 0.40), indicating the consistency of their network properties. The small-worldness for the oncological reference matrix was 1.95, for the HCP median

matrix was 2.07, and the Dice similarity was 0.63, further supporting the similarity between the two matrices. The pseudo-healthy reference created presented expected characteristics for a structural connectivity matrix. Given the similarity in graph properties between the median HCP-SC and SCnos pseudo-healthy matrices, it can be concluded that the pseudo-healthy reference is valid and can be confidently applied in the statistical analysis.

2.7 Statistical Analysis

For each subject, structural connectivity (SC) based on Number of streamlines (SCnos), similarity network fusion matrix for diffusion microstructure (SNFmicro), and functional connectivity (FC) matrices underwent individual standardization procedures (normalization to the range [0.01-0.99], inverse arctangent transformation, and z-scoring). Specifically, upper triangular matrices were normalized before reconstructing a square matrix, while connections with zero values were excluded to ensure reliability. In contrast, the Integration Connectivity (IC) matrix was derived simply by concatenating the already normalized SCnos, SNFmicro, and FC matrices without further processing. An equivalent procedure was applied to standardize pseudo-healthy SCnos, SNFmicro, FC and IC matrices.

2.8 Sensitivity Analysis

An IC-based sensibility analysis was performed for R^2 thresholds in the range [0.15:0.01:0.35] to highlight the cut-off impact. NADs obtained for IC with thresholds in the range were compared with the similarity structural index[31] (SSIM), and the multiscale structural similarity index[32] (MSSSIM). SSIM and MSSSIM values are within the range [0,1], where the higher the value, the better the overlap. Supplementary Fig. S9 outlines the alterations behaviours varying the R^2 threshold value. Panel A highlights the SSIM and MSSSIM indices between the distribution of NAD related to the IC modality derived from varying the cut-off value and the distribution of NAD related to the IC modality derived from the selected threshold equal to 0.25. It can be appreciated that NAD similarity is higher for thresholds higher than 0.25. Panel B shows the total number of altered networks across the subjects with the different thresholds, normalized by the number of altered networks among the patients derived from the selected cut-off. The plot highlights a linear trend.

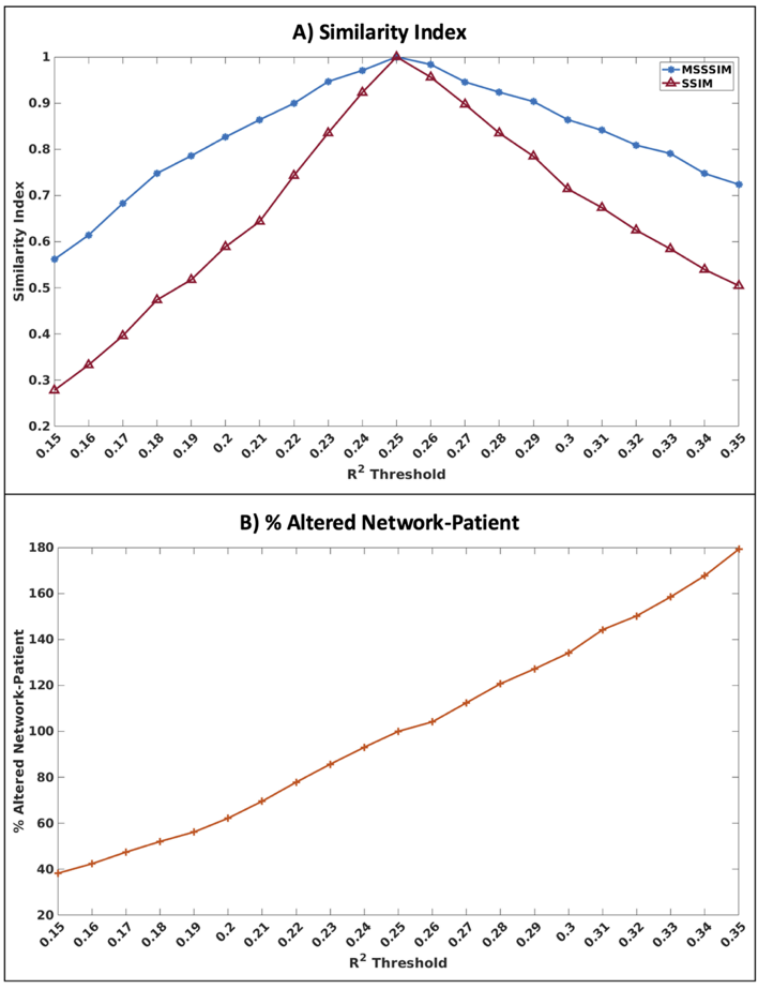

Supplementary Figure S9. *R^2 threshold Sensitivity Analysis. Sensitivity analysis results obtained changing the R^2 threshold in the range [0.15:0.01:0.35]. Above: Structural Similarity indices performed comparing the Networks Alteration Degree Matrices obtained with different thresholds with the Networks Alteration Degree Matrix obtained with a R^2 threshold equal to 0.25 (as reported in the manuscript). In blue are, Multiscale Structural Similarity Index (MSSSIM) results. In red are, Structural Similarity Index (SSIM) results. Both indexes highlight a higher similarity for thresholds quite near to the selected one. Below, plot representing the number of altered networks among all patients with the different thresholds, normalized by the number of altered networks across the patients obtained with the selected network. The higher the threshold, the higher the number of alterations.*

References:

1. Louis, D. N. *et al.* The 2016 World Health Organization Classification of Tumors of the Central Nervous System: a summary. *Acta Neuropathologica* vol. 131 803–820 Preprint at https://doi.org/10.1007/s00401-016-1545-1 (2016).
2. Harms, M. P. *et al.* Extending the Human Connectome Project across ages: Imaging protocols for the Lifespan Development and Aging projects. *Neuroimage* **183**, 972–984 (2018).
3. Glasser, M. F. *et al.* The minimal preprocessing pipelines for the Human Connectome Project. *Neuroimage* **80**, 105–124 (2013).
4. Jenkinson, M., Beckmann, C. F., Behrens, T. E. J., Woolrich, M. W. & Smith, S. M. FSL. *Neuroimage* **62**, 782–790 (2012).
5. van Wijk, B. C. M., Stam, C. J. & Daffertshofer, A. Comparing brain networks of different size and connectivity density using graph theory. *PLoS One* **5**, (2010).

6. de Brito Robalo, B. M. *et al.* Improved sensitivity and precision in multicentre diffusion MRI network analysis using thresholding and harmonization. *Neuroimage Clin* **36**, (2022).
7. Zhang, H., Schneider, T., Wheeler-Kingshott, C. A. & Alexander, D. C. NODDI: Practical in vivo neurite orientation dispersion and density imaging of the human brain. *Neuroimage* **61**, 1000–1016 (2012).
8. Tustison, N. J. *et al.* N4ITK: improved N3 bias correction. *IEEE Trans Med Imaging* **29**, 1310–1320 (2010).
9. Doshi, J., Erus, G., Ou, Y., Gaonkar, B. & Davatzikos, C. Multi-atlas skull-stripping. *Acad Radiol* **20**, 1566–1576 (2013).
10. Ashburner, J. & Friston, K. J. Unified segmentation. *Neuroimage* **26**, 839–851 (2005).
11. Fonov, V. *et al.* Unbiased average age-appropriate atlases for pediatric studies. *Neuroimage* **54**, 313–327 (2011).
12. Andersen, S. M., Rapcsak, S. Z. & Beeson, P. M. Cost function masking during normalization of brains with focal lesions: still a necessity? *Neuroimage* **53**, 78–84 (2010).
13. Smith, S. M. *et al.* Advances in functional and structural MR image analysis and implementation as FSL. in *NeuroImage* vol. 23 (2004).
14. Andersson, J. L. R., Skare, S. & Ashburner, J. How to correct susceptibility distortions in spin-echo echo-planar images: Application to diffusion tensor imaging. *Neuroimage* **20**, 870–888 (2003).
15. Jenkinson, M., Bannister, P., Brady, M. & Smith, S. Improved Optimization for the Robust and Accurate Linear Registration and Motion Correction of Brain Images. *Neuroimage* **17**, 825–841 (2002).
16. Greve, D. N. & Fischl, B. Accurate and robust brain image alignment using boundary-based registration. *Neuroimage* **48**, 63–72 (2009).
17. Salimi-Khorshidi, G. *et al.* Automatic denoising of functional MRI data: Combining independent component analysis and hierarchical fusion of classifiers. *Neuroimage* **90**, 449–468 (2014).
18. Griffanti, L. *et al.* ICA-based artefact removal and accelerated fMRI acquisition for improved resting state network imaging. *Neuroimage* **95**, 232–247 (2014).
19. Damaraju, E. *et al.* Dynamic functional connectivity analysis reveals transient states of dysconnectivity in schizophrenia. *Neuroimage Clin* **5**, 298–308 (2014).
20. Silvestri, E. *et al.* Widespread cortical functional disconnection in gliomas: an individual network mapping approach. *Brain Commun* **4**, (2022).
21. Jo, H. J. *et al.* Effective preprocessing procedures virtually eliminate distance-dependent motion artifacts in resting state FMRI. *J Appl Math* **2013**, (2013).
22. Power, J. D., Barnes, K. A., Snyder, A. Z., Schlaggar, B. L. & Petersen, S. E. Spurious but systematic correlations in functional connectivity MRI networks arise from subject motion. *Neuroimage* **59**, 2142–2154 (2012).
23. Tournier, J. D., Mori, S. & Leemans, A. Diffusion tensor imaging and beyond. *Magnetic Resonance in Medicine* vol. 65 1532–1556 Preprint at https://doi.org/10.1002/mrm.22924 (2011).
24. Bastiani, M. *et al.* Automated quality control for within and between studies diffusion MRI data using a non-parametric framework for movement and distortion correction. *Neuroimage* **184**, 801–812 (2019).
25. Tournier, J.-D. *et al.* MRtrix3: A fast, flexible and open software framework for medical image processing and visualisation. *Neuroimage* **202**, 116137 (2019).
26. Veraart, J. *et al.* Denoising of diffusion MRI using random matrix theory. *Neuroimage* **142**, 394–406 (2016).
27. Andersson, J. L. R. & Sotiropoulos, S. N. An integrated approach to correction for off-resonance effects and subject movement in diffusion MR imaging. *Neuroimage* **125**, 1063–1078 (2016).
28. Avants, B. B. *et al.* A reproducible evaluation of ANTs similarity metric performance in brain image registration. *Neuroimage* **54**, 2033–2044 (2011).
29. Jeurissen, B., Tournier, J.-D., Dhollander, T., Connelly, A. & Sijbers, J. Multi-tissue constrained spherical deconvolution for improved analysis of multi-shell diffusion MRI data. *Neuroimage* **103**, 411–426 (2014).
30. Steven, A. J., Zhuo, J. & Melhem, E. R. Diffusion Kurtosis Imaging: An Emerging Technique for Evaluating the Microstructural Environment of the Brain. *American Journal of Roentgenology* **202**, (2013).
31. Bovik, A., Wang, Z. & Sheikh, H. Structural Similarity Based Image Quality Assessment. in 225–241 (2005). doi:10.1201/9781420027822.ch7.
32. Wang, Z., Simoncelli, E. P. & Bovik, A. C. Multiscale structural similarity for image quality assessment. in *The Thrity-Seventh Asilomar Conference on Signals, Systems & Computers, 2003* 1398–1402 (IEEE, 2003). doi:10.1109/ACSSC.2003.1292216.